Electronic Supplementary Material (ESI) for Journal of Materials Chemistry C.
This journal is © The Royal Society of Chemistry 2020

Supplementary Information

Silicon-compatible Optoelectronic Artificial Neuron

Zhengyuan Liu[1], Bingcheng Luo[1], Danyang Wang[2]*

[1]School of Physical Science and Technology, Northwestern Polytechnical University, Xi'an, Shaanxi, 710072, China

[2]School of Materials Science and Engineering, The University of New South Wales, Sydney, NSW 2052, Australia

[*]Electronic mail: luobingcheng@nwpu.edu.cn

1. Characterization of the as-deposited *a*-MoSi thin films

Figure S1(a) shows the surface morphology for the *a*-MoSi thin film captured by an atomic force microscope (AFM, Bruker Dimension Icon). The sample shows crack-free and uniform microstructure with a root mean squared surface roughness of 0.35 nm. The valence state and presence of elements were examined by X-ray photoelectron spectroscopy (XPS, Thermo SCIENTIFIC ESCALAB 250Xi). Figure S1(b) depicts the XPS spectrum of the *a*-MoSi thin film, confirming the presence of Si and Mo elements. The highly symmetric peak located at ~103 eV on Si 2p XPS spectrum (Figure S1(c)) suggests the -4 valence state of silicon.[1] The spin–orbit splitting energy (~3.15 eV) of Mo 3d (Figure S1(d)) is consistent with previously reported data for Mo^{4+}.[2] Figure S1(e) shows grazing incidence X-ray diffraction

(GIXRD, PANalytical X'Pert PRO) pattern of *a*-MoSi thin film. No characteristic peaks were visible, echoing the amorphous nature of the thin film. Thickness of the *a*-MoSi thin films was determined by fitting the data obtained from Ellipsometry (Mikropack SpecEI-2000-VIS). Thicknesses of the three films were found to be Sample #1 ~117.7 nm (Figure S1(f)), Sample #2 ~213.5 nm (Figure S1(g)) and Sample #3 ~346.1 nm (Figure S1(h)), respectively. In order to crosscheck the accuracy of the fitting results, the cross-section scanning electron microscope (SEM, FEI Verios G4) image of Sample #2 was employed. As shown in Figure S1(i), *a*-MoSi layer was ~207 nm, which highly is consistent with our fitting results.

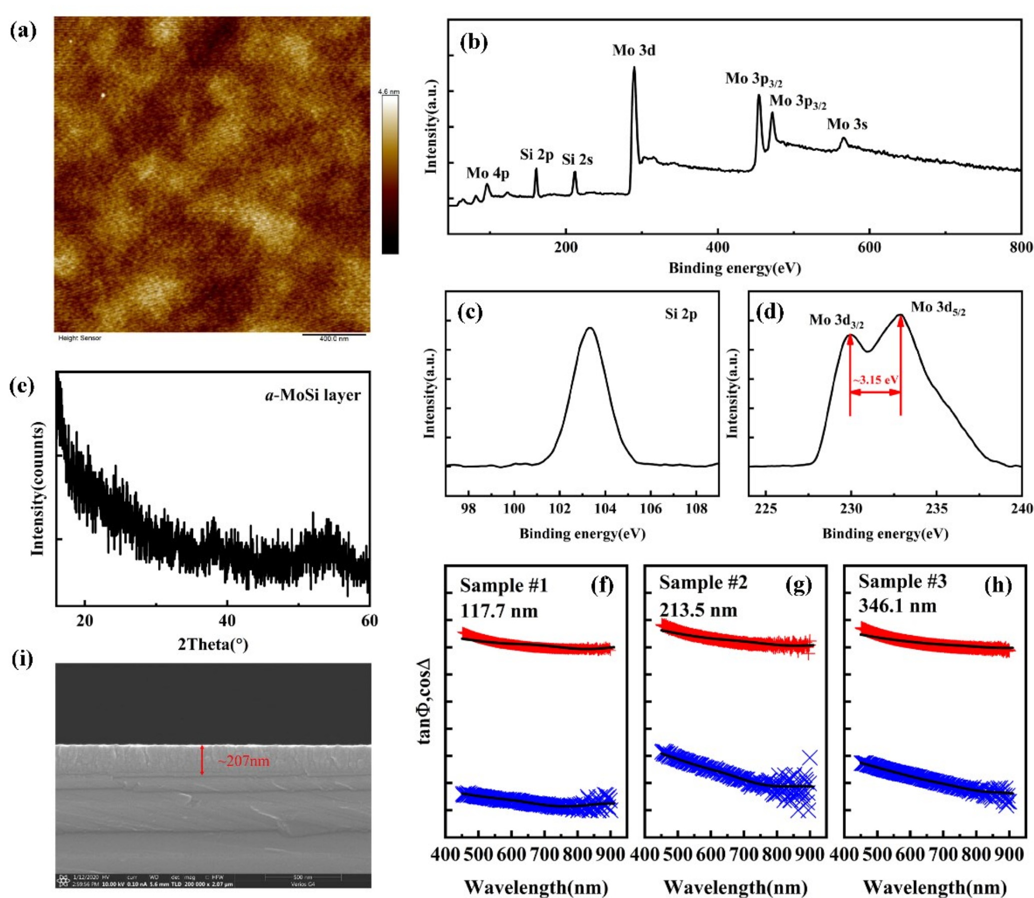

Figure S1 Characterization of as-deposited *a*-MoSi thin films. (a) AFM

topographical image of *a*-MoSi thin film. (b) Wide-scan XPS survey of *a*-MoSi thin film. (c) High-resolution Si 2p XPS spectrum and (d) High-resolution Mo 3d XPS spectrum. (e) GIXRD pattern of *a*-MoSi thin film. (f)-(h) Ellipsometric spectrum of *a*-MoSi thin films with different thicknesses. The black solid lines are the fitting results. (i) Cross-section SEM image of *a*-MoSi thin film.

2. Origin of Negative Photoconductivity (NPC) in designed artificial neuron

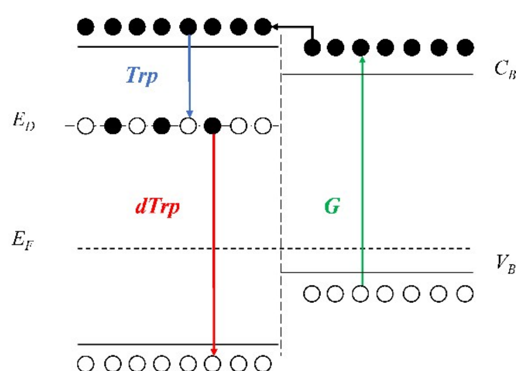

Figure S2 Proposed energy level diagram explaining the origin of NPC in designed artificial neuron.

The origin of NPC and the PPC/NPC conversion could be ascribed to the trade-off between electron trapping and detrapping dynamics related to a shallow defect level. Here we propose a concise diagram to understand the electron trapping/detrapping dynamics, as shown in **Figure S2**. The physical processes including electron-hole generation, thermalization, recombination, trapping and detrapping in designed

artificial neuron under laser illumination are considered. Firstly, electrons in the silicon valence band (right side) are excited by light (shown by green arrow) and forced into the conduction band of a-MoSi (left side) by applied electric field. Some of the excited electrons are trapped by the defect energy level (shown by blue arrow) and the other carriers move to the band-edge, *i.e.*, the thermalization process. Both processes can be described as:[3]

$$\frac{dn_{ph}}{dt} = G - \frac{n_{ph}}{\tau_{th}} - \frac{n_{ph}}{\tau_{trp}}\left(1 - \frac{n_{trp}}{N_{trp}}\right) \tag{1}$$

$$\frac{dp_{ph}}{dt} = G - \frac{p_{ph}}{\tau_{th}} \tag{2}$$

where n_{ph} is the density of excited electrons, p_{ph} the density of holes, N_{trp} the concentration of traps, n_{trp} the concentration of trapped electrons, τ_{th} the carrier thermalization time and τ_{trp} the carrier trapping time.

Subsequently, excited electrons and holes near the band-edge would recombine, and the trapped electrons can detrap to the valence band due to their instability and the electrostatic effect of other trapped electrons (shown by the red arrow). The change of band-edge carrier concentration can be expressed as:[3]

$$\frac{d\Delta n}{dt} = \frac{n_{ph}}{\tau_{th}} - \frac{\Delta n}{\tau_r} + \frac{n_{trp}}{\tau_{dtrp}} \tag{3}$$

$$\frac{d\Delta p}{dt} = \frac{p_{ph}}{\tau_{th}} - \frac{\Delta n}{\tau_r} \tag{4}$$

where Δn and Δp are the changes of band-edge electron and hole concentrations,

respectively, and τ_r is the band-edge carrier recombination lifetime. Therefore, the change of trapped electron concentration can be expressed as:

$$\frac{dn_{trp}}{dt} = \frac{n_{ph}}{\tau_{trp}}\left(1 - \frac{n_{trp}}{N_{trp}}\right) \tag{5}$$

Due to the rather fast NPC response (~10^{-4} s), the variation in carrier mobility can be ignored[4] and thereby one can assume that the carrier mobility remains unchanged in the artificial neuron. Accordingly, the photoconductivity can be expressed as:

$$\Delta\sigma = e\mu_n(\Delta n + n_{ph}) + e\mu_p(\Delta p + p_{ph}) \tag{6}$$

where μ_n and μ_p are the mobility of electron and hole, respectively.

When the bias voltage is small (corresponding to low-level injection), traps are partially occupied by the excited electrons, *i.e.*, $n_{trp} < N_{trp}$, Equation (6) can be transformed into:

$$\Delta\sigma = -Ge\mu_n\frac{\tau_{th}\tau_{dtrp}}{\tau_{th} + \tau_{trp}} + e(\mu_n + \mu_p)G(\tau_{th} + \tau_r) \tag{7}$$

When the two terms of the right hand side of Equation (7) are identical, $\Delta\sigma$ equals zero. Thus Equation (7) is simplified as

$$\frac{\tau_{dtrp}}{\tau_{th} + \tau_{trp}} = \left(1 + \frac{\mu_p}{\mu_n}\right)(1 + \frac{\tau_r}{\tau_{th}}) \tag{8}$$

Since the experimentally determined value of τ_{trp} (~10^{-4} s) is much larger than τ_{th} (~10^{-6} s),[5, 6] Equation (8) can be further simplified to

$$\frac{\tau_{dtrp}}{\tau_{trp}} = \left(1 + \frac{\mu_p}{\mu_n}\right)(1 + \frac{\tau_r}{\tau_{th}}) \quad (9)$$

Referring to previous results,[7-10] both $\left(1 + \frac{\mu_p}{\mu_n}\right)$ and $\left(1 + \frac{\tau_r}{\tau_{th}}\right)$ are slightly greater than 1. Therefore, if the ratio of detrapping time and trapping time is larger than 1, then an NPC occurs. Conversely, a PPC is resulted.

When traps are completely occupied by the excited electrons under large bias voltage, *i.e.*, $n_{trp} \approx N_{trp}$, Equation (6) can be re-written as:

$$\Delta\sigma = -e\mu_n N_{trp} + e(\mu_n + \mu_p)G(\tau_{th} + \tau_r) \quad (10)$$

Obviously, the first term on the right hand side of Equations (10) corresponds to NPC component, which is determined by the trap concentration and carrier mobility in the material. Further increase in laser intensity can boost up the second term, leading to a PPC.

In summary, PPC and NPC can be differentiated from one another based on their mechanisms and outputs. On the one hand, the well-known photoelectric effect, which is the origin of PPC, is often present in semiconductor materials.[11] When the incoming photon energy is greater than the bandgap energy of a solid state material, the electron in the valence band will be excited into the conduction band, resulting in a higher conductivity, *i.e.*, PPC. On the other hand, in amorphous semiconductors, the absence of ligand atoms can cause some dangling bonds in the material[12]. Some energy levels near the center of the bandgap will be created because the atoms

associated with these dangling bonds are usually considered as isolated atoms. The exact location of these energy levels is determined by the chargeability of the material. Because the electron wave function at these energy levels is localized, they are often named as ‘trap’ energy levels, *i.e.*, the electrons are confined to these levels as if they had fallen into traps. Particularly, the presence of shallow trap energy levels will enable a diametrically opposite photoconduction in amorphous semiconductors. If the excited electrons are trapped by the shallow trap energy levels, whose electrostatic potential energy will greatly reduce the concentration of electrons in the conduction band, the material becomes more resistive, *i.e.*, NPC.

3. Photoconductivity for silicon substrates

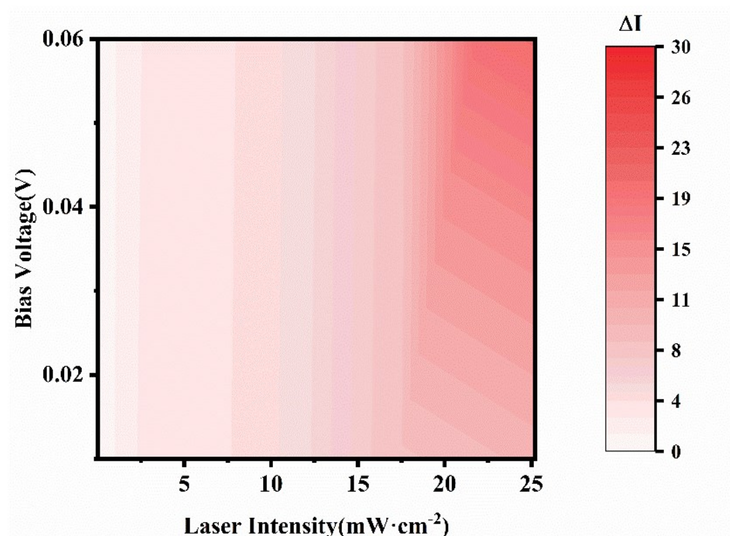

Figure S3 Photoconductivity response characteristics of silicon substrate under the dual optical-electrical regulation.

The photoconductivity response characteristics of the silicon substrate (**Figure S3**) under 532 nm laser illumination was measured to eliminate its influence on photoconductivity results of our devices. The silicon substrate shows a PPC behavior merely under 532 nm laser illumination, which is common for semiconductors.[11] Thus, the contribution of the silicon substrate to the observed NPC in our device is negligible.

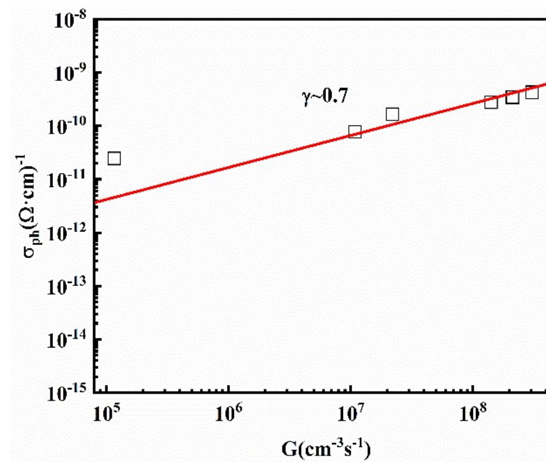

Figure S4 Room temperature G-dependent photoconductivity. The 532 nm laser intensity was set to minimum (9.6 $\mu W\cdot cm^{-2}$) to suppress the heating effect.

In addition, we obtained the dependence of photoconductivity on *G* at room temperature, as shown in **Figure S4**, which supports the results we obtained in Figure 1(c).

4. Photoconductivity for devices with different *a*-MoSi layer thicknesses

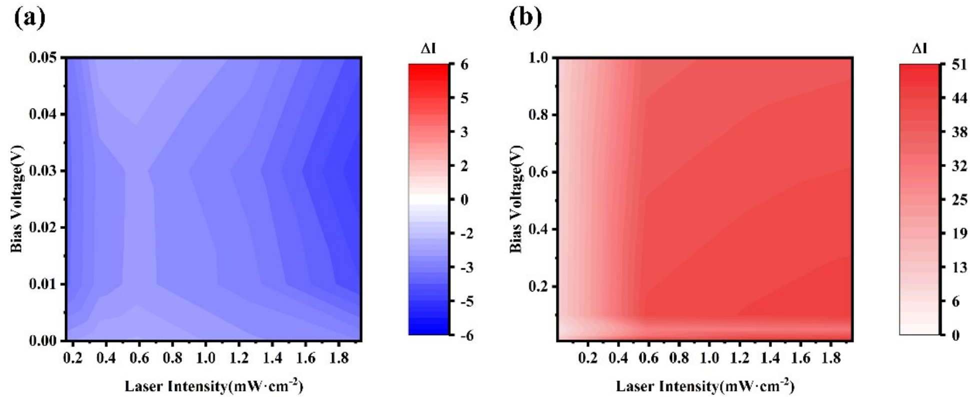

Figure S5 Photoconductivity response characteristics of devices with different *a*-MoSi layer thicknesses. (a) Sample #1 and (b) Sample #3.

In addition to the device with *a*-MoSi layer thickness of ~200±10 nm (Sample #2) focused on in the main manuscript, the photoconductivity response characteristics of two other devices (Sample #1 and Sample #3) with different *a*-MoSi layer thicknesses under 405 nm laser illumination were also measured, as shown in **Figure S5**. Obviously, a too thin (or too thick) *a*-MoSi layer suppresses the occurrence of the NPC/PPC conversion. This means that only the device with suitable *a*-MoSi layer thickness could provide an injection level for the NPC/PPC conversion, because the partial voltage falling on the *a*-MoSi layer is determined by the layer thickness.

References

1. A. Kitao, K. Imakita, I. Kawamura and M. Fujii, *Journal of Physics D: Applied Physics*, 2014, **47**, 215101.

2. J. G. Choi and L. T. Thompson, *Applied Surface Science*, 1996, **93**, 143-149.
3. Y. Yang, X. Peng, H.-S. Kim, T. Kim, S. Jeon, H. K. Kang, W. Choi, J. Song, Y.-J. Doh and D. Yu, *Nano Letters*, 2015, **15**, 5875-5882.
4. P.-C. Wei, S. Chattopadhyay, M.-D. Yang, S.-C. Tong, J.-L. Shen, C.-Y. Lu, H.-C. Shih, L.-C. Chen and K.-H. Chen, *Physical Review B*, 2010, **81**, 045306.
5. M. S. Tyagi and R. Van Overstraeten, *Solid-State Electronics*, 1983, **26**, 577-597.
6. J. A. del Alamo and R. M. Swanson, *Solid-State Electronics*, 1987, **30**, 1127-1136.
7. F. J. Morin and J. P. Maita, *Physical Review*, 1954, **96**, 28-35.
8. R. A. Logan and A. J. Peters, *Journal of Applied Physics*, 1960, **31**, 122-124.
9. P. Norton, T. Braggins and H. Levinstein, *Physical Review B*, 1973, **8**, 5632-5653.
10. C. Canali, C. Jacoboni, F. Nava, G. Ottaviani and A. Alberigi-Quaranta, *Physical Review B*, 1975, **12**, 2265-2284.
11. N. V. Joshi, *Photoconductivity: Art: Science & Technology*, Taylor & Francis, 1990.
12. J. Singh and K. Shimakawa, *Advances in Amorphous Semiconductors*, CRC Press, 2003.